The Astrophysical Journal Letters, 921:L43 (9pp), 2021 November 10 https://doi.org/10.3847/2041-8213/ac32dc
© 2021. The Author(s). Published by the American Astronomical Society.
OPEN ACCESS

Implications of Eccentric Observations on Binary Black Hole Formation Channels

Michael Zevin[1,2,7], Isobel M. Romero-Shaw[3,4], Kyle Kremer[5,6], Eric Thrane[3,4], and Paul D. Lasky[3,4]
[1] Kavli Institute for Cosmological Physics, The University of Chicago, 5640 South Ellis Avenue, Chicago, IL 60637, USA; michaelzevin@uchicago.edu
[2] Enrico Fermi Institute, The University of Chicago, 933 East 56th Street, Chicago, IL 60637, USA
[3] School of Physics and Astronomy, Monash University, VIC 3800, Australia
[4] OzGrav: The ARC Centre of Excellence for Gravitational Wave Discovery, Clayton, VIC 3800, Australia
[5] TAPIR, California Institute of Technology, Pasadena, CA 91125, USA
[6] The Observatories of the Carnegie Institution for Science, Pasadena, CA 91101, USA
Received 2021 September 23; revised 2021 October 15; accepted 2021 October 24; published 2021 November 11

Abstract

Orbital eccentricity is one of the most robust discriminators for distinguishing between dynamical and isolated formation scenarios of binary black hole mergers using gravitational-wave observatories such as LIGO and Virgo. Using state-of-the-art cluster models, we show how selection effects impact the detectable distribution of eccentric mergers from clusters. We show that the observation (or lack thereof) of eccentric binary black hole mergers can significantly constrain the fraction of detectable systems that originate from dynamical environments, such as dense star clusters. After roughly 150 observations, observing no eccentric binary signals would indicate that clusters cannot make up the majority of the merging binary black hole population in the local universe (95% credibility). However, if dense star clusters dominate the rate of eccentric mergers and a single system is confirmed to be measurably eccentric in the first and second gravitational-wave transient catalogs, clusters must account for at least 14% of detectable binary black hole mergers. The constraints on the fraction of detectable systems from dense star clusters become significantly tighter as the number of eccentric observations grows and will be constrained to within 0.5 dex once 10 eccentric binary black holes are observed.

Unified Astronomy Thesaurus concepts: Gravitational wave sources (677); Gravitational waves (678); Astrophysical black holes (98); Stellar mass black holes (1611); Gravitational wave astronomy (675)

1. Introduction

In the past few years, the dramatic increase in compact binary mergers observed by gravitational-wave (GW) detectors has fueled immense interest and debate regarding compact binary formation pathways, particularly for binary black hole (BBH) systems. Over a dozen potential formation scenarios for the BBH mergers observed by the LIGO–Virgo detector network (Aasi et al. 2015; Acernese et al. 2015) have been proposed, including isolated massive-star binary progenitors (e.g., Bethe & Brown 1998; Dominik et al. 2012; Belczynski et al. 2016; Bavera et al. 2021), assembly in dynamical environments (e.g., Portegies Zwart & McMillan 2000; O'Leary et al. 2006; Downing et al. 2010; Rodriguez et al. 2016; Banerjee 2017; Di Carlo et al. 2019), gas-driven assembly and orbital evolution (e.g., McKernan et al. 2014; Bartos et al. 2017; Stone et al. 2017), and primordial origins (e.g., Bird et al. 2016; Sasaki et al. 2018; Clesse & Garcia-Bellido 2020; Franciolini et al. 2021). Given the heterogeny of the compact binary coalescences observed to date, a mix of formation channels is currently preferred over a single channel dominating the formation of merging BBH systems in the universe (Abbott et al. 2021a; Bouffanais et al. 2021; Wong et al. 2021; Zevin et al. 2021).

Though population-based studies offer insights into the broad features of BBH formation, the most efficient means of constraining formation scenarios is to identify features of BBH systems unique to particular channels. One such key feature is orbital eccentricity. Compact binary systems that inspiral over long timescales efficiently damp orbital eccentricity through angular momentum loss from GW emission (Peters 1964). Therefore, even field binaries born with high eccentricity are nearly circular by the time they enter the LIGO–Virgo sensitive frequency band. For example, a BBH composed of two 20 $M_\odot$ black holes (BHs) at an initial orbital separation of 1 $R_\odot$ and initial eccentricity of 0.9 (0.99) will have an eccentricity at a GW frequency of 10 Hz of 0.001 (0.05) and merge in 32 yr (6 days). The only means of producing measurably eccentric BBH mergers in the LIGO–Virgo band that does not require a high degree of fine-tuning is through strong gravitational encounters in dynamical environments (e.g., O'Leary et al. 2009; Kocsis & Levin 2012; Samsing et al. 2014; Samsing et al. 2018; Samsing 2018; Gondán et al. 2018; Rodriguez et al. 2018b; Takatsy et al. 2019; Zevin et al. 2019; Rasskazov & Kocsis 2019; Gröbner et al. 2020; Samsing et al. 2020b; Gondán & Kocsis 2021; Tagawa et al. 2021) or channels that can pump eccentricity into inspiraling binaries, such as the secular evolution of hierarchical systems (e.g., Antonini & Perets 2012; Antognini et al. 2014; Silsbee & Tremaine 2017; Antonini et al. 2017; Rodriguez & Antonini 2018; Fragione & Bromberg 2019; Fragione & Kocsis 2019; Liu et al. 2019; Liu & Lai 2019) or perturbations of wide triples in the Galactic field from flyby encounters (e.g., Michaely & Perets 2019, 2020).

Orbital eccentricity is arguably the most robust discriminator for distinguishing between isolated and dynamical BBH formation scenarios; so long as BHs form in clusters and are not kicked out of clusters at formation, highly eccentric mergers are an inevitable by-product of two-body relaxation and small-N dynamics (Samsing et al. 2014; Rodriguez et al. 2018b). In classical globular clusters (GCs), which are perhaps the best-studied environment of eccentric mergers from strong gravitational encounters, the presence of BHs is evidenced both observationally (through detection of BH binary candidates in several Milky Way GCs; Strader et al. 2012;

[7] NASA Hubble Fellow.

Original content from this work may be used under the terms of the Creative Commons Attribution 4.0 licence. Any further distribution of this work must maintain attribution to the author(s) and the title of the work, journal citation and DOI.

Giesers et al. 2018, 2019) and computationally through *N*-body modeling (Mackey et al. 2007; Breen & Heggie 2013; Wang et al. 2016; Kremer et al. 2018, 2019; Arca Sedda et al. 2018; Antonini & Gieles 2020a; Weatherford et al. 2020; Kremer et al. 2020). Eccentric mergers from strong gravitational encounters have been shown both semianalytically and numerically to account for ≈10% of the underlying population of BBH mergers in GCs, with approximately half of these having eccentricities $\geqslant 0.1$ at a GW frequency of 10 Hz, the lower edge of the LIGO–Virgo band (Samsing & Ramirez-Ruiz 2017; Samsing et al. 2018; Samsing 2018; Rodriguez et al. 2018b; Zevin et al. 2019; Kremer et al. 2020; Antonini & Gieles 2020b).

Despite the robust theoretical predictions for generating eccentric BBH mergers in clusters, the implications that such a detection would have on constraining BBH formation scenarios depends sensitively on the interplay between the measurability and detectability of such systems. Eccentricity acts as a double-edged sword; larger eccentricities are easier to distinguish from their circular counterparts using parameter estimation, though there is an inherent selection bias impinging on the detection of eccentric sources due to the template banks used for matched-filter searches for GW signals, which typically assume quasi-circular aligned-spin binaries (Hooper et al. 2012; Allen et al. 2012; Dal Canton et al. 2014; Usman et al. 2016; Adams et al. 2016; Messick et al. 2017; Nitz et al. 2017; Chu et al. 2020; Davies et al. 2020; Aubin et al. 2021). Though burst searches may be used to detect unmodeled sources, such as highly eccentric mergers (Tiwari et al. 2016; Abbott et al. 2019a; Ramos-Buades et al. 2020), they are less capable of digging deep into the noise for signal, and their sensitivity is more difficult to quantify (Klimenko et al. 2016). In terms of measurability, BBH systems with properties similar to GW150914 (Abbott et al. 2016) can be distinguished as eccentric if their eccentricities are $\gtrsim 0.05$ at a GW frequency of 10 Hz (Lower et al. 2018), consistent with the upper limits on orbital eccentricity (Romero-Shaw et al. 2019) for the events in the first LIGO–Virgo GW transient catalog (GWTC-1; Abbott et al. 2019b).[8] However, even if an eccentric GW source were detected, there is currently no published selection function for eccentric sources to translate this detection into characteristics of the source population, such as the merger rate. This is in part because of the difficulty in modeling eccentric signals (Loutrel 2020) and the computational burden of adding an extra dimension to matched-filter template banks.

In this Letter, we quantify how the detection of an eccentric BBH merger (or lack thereof) impacts the inferred fraction of BBH mergers originating from dense stellar clusters[9] by approximating selection effects that account for eccentricity in a realistic cluster population. With selection effects and measurability of eccentric sources accounted for, and assuming that dense star clusters dominate the rate of measurably eccentric BBH mergers, the robustness of eccentricity predictions from cluster modeling allows for constraints to be placed on the relative contribution of BBH mergers from clusters as a whole. In Section 2, we describe the cluster models used as a basis in this analysis. Section 3 covers the determination of selection effects for generically eccentric systems and our assumptions regarding the ability of eccentric sources to be distinguished from circular. Our main results are presented in Section 4, which quantifies the constraints that a bona fide eccentric detection will have on the contribution of dynamical channels to the underlying population of BBH systems in the context of both the current catalogs of GWs and future observations. We summarize our results and discuss the caveats of our analysis in Section 5. We use a flat ΛCDM cosmology with Planck 2015 cosmological parameters (Ade et al. 2016) throughout this work.

2. Cluster Models

We use dense star cluster models from the `CMC Cluster Catalog` (Kremer et al. 2020) to construct our population of dynamical BBH mergers. Collectively, these models span roughly the full parameter space of the Milky Way GCs (in cluster mass, core/half-light radius, metallicity, and position within the Galactic potential) and include state-of-the-art prescriptions for stellar evolution and BH formation (see Kremer et al. 2020, for more details). Importantly, strong binary-mediated gravitational encounters are modeled with direct integration using `Fewbody` (Fregeau et al. 2004; Fregeau & Rasio 2007) with updates to include post-Newtonian terms for dynamical encounters involving BHs (Rodriguez et al. 2018a, 2018b).

The gravitational radiation reaction, which enters at the 2.5 post-Newtonian order, is crucial for the formation of high-eccentricity BBH mergers in clusters (Samsing et al. 2014; Samsing & Ramirez-Ruiz 2017; Rodriguez et al. 2018b; Zevin et al. 2019). During strong gravitational encounters between single and/or binary BH systems, component BHs can undergo dozens of partner swaps, forming hardened temporary binaries that have eccentricities e drawn from a "quasi-thermal" distribution (the probability density is proportional to e). If this intermediate-state binary has a large enough orbital eccentricity, the efficient loss of orbital energy from GWs during close periapse passages leads to a rapid merger on a timescale of days with significant eccentricity in the sensitive frequency ranges of ground-based GW detectors. In addition, classically unbound BHs can lose enough orbital energy from close passages during these encounters to become bound and rapidly merge. This can also occur between two single BHs in the cluster if the impact parameter is small enough, though this subchannel produces BBH mergers with eccentricities more accessible in the decihertz regime (Samsing et al. 2020a).

These merger channels from strong gravitational encounters are collectively referred to as GW captures and have significantly larger eccentricities compared to BBH mergers that were ejected from the cluster due to a prior dynamical interaction or BBHs that merge between strong gravitational encounters (Samsing 2018; Rodriguez et al. 2018a; Zevin et al. 2019). Figure 1 shows normalized eccentricity distributions for BBHs in our astrophysically weighted cluster models at a reference GW frequency of 10 Hz, $e_{10\,\mathrm{Hz}}$, both with and without the inclusion of selection effects (described in detail in the next section). The local BBH merger rate from all subchannels in this model is $20\,\mathrm{Gpc^{-3}\,yr^{-1}}$. Further details regarding the cluster population and determination of BBH eccentricities can be found in Appendix A.

[8] There are claims that eccentric BBH mergers have been observed in the most recent observing run (Romero-Shaw et al. 2020; Gayathri et al. 2020; Romero-Shaw et al. 2021), although the interpretation for certain systems, such as GW190521, is speculative. We discuss this further in Sections 4 and 5.

[9] We use the term "dense star clusters" to denote clusters with masses in the range of $\approx 10^5$–$10^7\,M_\odot$ and virial radii of ≈0.5–5 pc. Critically, however, we do not limit this definition to only old low-metallicity clusters that survive to the present day, like traditional GCs. We also incorporate high-metallicity clusters born relatively recently (essential for producing lower-mass BH mergers; Chatterjee et al. 2017), as well as disrupted clusters that do not survive to the present day (inclusion of these disrupted clusters may increases the total BBH merger rate from clusters by a factor of ≈2; e.g., Rodriguez & Loeb 2018; Fragione & Kocsis 2018).

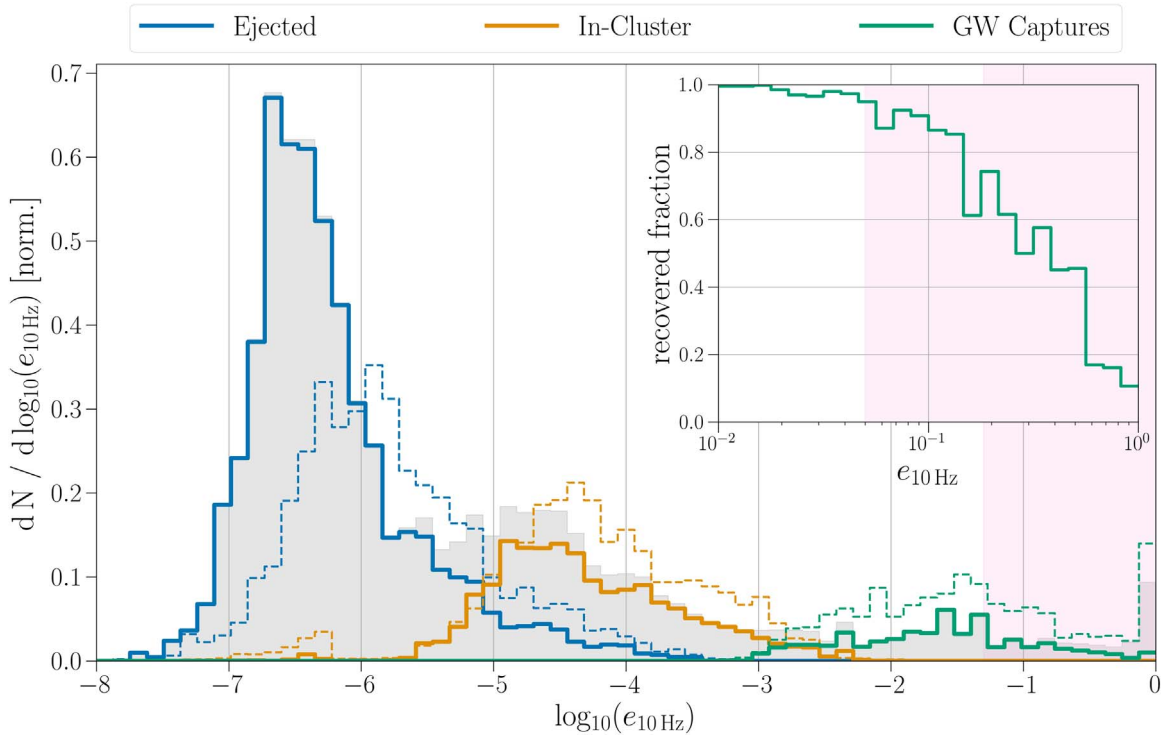

Figure 1. Eccentricity distributions for detectable BBH mergers assuming perfectly matching templates (gray shading), circular templates (solid lines), and neglecting detection probabilities $p_{\rm det}$ altogether (dashed lines). Colored lines denote whether the BBH system was ejected from the cluster (blue), merged inside the cluster between strong dynamical interactions (orange), or merged as a capture during a strong gravitational encounter (green). The difference between the background gray histogram and the solid-line histogram for the GW capture population shows the systems that are "missed" by searching with circular templates; this recovered fraction is also shown in the inset panel as a function of eccentricity. The detectable distribution assuming circular templates is normalized to the detectable distribution assuming perfectly matching templates to better visualize this difference; thus, the solid-line histograms integrate to slightly less than unity. The pink shaded region marks systems with $e_{10\,\rm Hz} > 0.05$, the approximate eccentricity requirement for distinguishing GW150914-like systems from circular. Ejected mergers are more prevalent in the detectable distribution because more massive systems are ejected earlier in the history of the cluster and have longer inspiral timescales so that they can readily merge in the local universe.

3. Selection Effects and Measurability of Eccentric Sources

Due to the lack of large-scale injection campaigns that have the ability to determine a sensitive spacetime volume for eccentric sources, we instead estimate detection probabilities using a fixed signal-to-noise ratio (S/N) threshold required for detection. For all S/N calculations, we use the waveform approximant `TEOBResumS` (Damour & Nagar 2014; Nagar et al. 2018), which is a time-domain effective one-body approximant (Buonanno & Damour 1999, 2000; Damour et al. 2000; Damour 2001; Damour et al. 2015) that can account for orbital eccentricity in the inspiral. `TEOBResumS` agrees well with numerical relativity (NR) for eccentricities of $e \lesssim 0.3$ at apastron frequency $\omega_a^{\rm EOB} \sim 0.03$ (which corresponds to a GW frequency of $\approx$10 Hz for a BBH with a total mass of $60\,M_\odot$; Chiaramello & Nagar 2020; Albanesi et al. 2021; Nagar et al. 2021), and, though untested for larger eccentricities due to a lack of available NR waveforms for comparison, it is physically valid even at high eccentricities of $e_{10\,\rm Hz} \simeq 0.9$.[10]

For each system, we calculate three separate time- and phase-maximized S/Ns with different assumptions: (1) the system is circular ($e_{10\,\rm Hz} = 0$) and the template is a perfectly matching circular template, (2) the system is eccentric with $e_{10\,\rm Hz} > 0$ and the template is a perfectly matching eccentric template, and (3) the system is eccentric with $e_{10\,\rm Hz} > 0$ and the template is a circular template with all other source properties identical. The first two of these correspond to the "optimal S/N" in the circular and eccentric cases, respectively, while the third characterizes the loss of signal from waveform mismatch.[11] In Figure 2, we show both the maximized matched-filter S/N and the detection probability for an exemplary BBH system over a range of eccentricities when entering the LIGO–Virgo band. Further details on S/N calculations and determination of detection probabilities are in Appendix B.

In addition to the detection probability of eccentric sources, another important aspect of this analysis is determining the minimum eccentricity that is required for parameter estimation routines to be able to confidently distinguish a system as eccentric. For systems with properties similar to GW150914, Lower et al. (2018) found this threshold eccentricity to be $e_{\rm thresh} \simeq 0.05$. This is consistent with the eccentricity upper limits for GWTC-1 events from Romero-Shaw et al. (2019). Due to the computational expense of performing eccentric

[10] Different waveform models use different definitions of eccentricity. When comparing predictions made with `TEOBResumS` to detections made with other approximants, care should be taken to ensure that the definition of eccentricity is consistent between models. One element of an eccentric waveform model that can be varied is the point at which the reference frequency is defined, since this varies from apoastron to periastron. By default, `TEOBResumS` defines the eccentricity at a reference frequency equivalent to that of a circular Keplerian orbit with radius equal to the semimajor axis of the eccentric binary. At low frequencies and eccentricities, this is similar to the eccentricity-dependent peak frequency from Wen (2003) used in the `CMC Cluster Catalog`; with eccentricity defined at a Keplerian reference frequency of 10 Hz, the difference between the two frequencies is $\lesssim$3 Hz (0.6 Hz) for $e_{10} \lesssim 0.2$ (0.05).

[11] A higher maximal S/N may be achieved in the third case through marginalization over the intrinsic parameters of the template, making our maximal matched-filter S/Ns a conservative lower limit. However, additional factors that may increase our estimated S/Ns will alter the results by less than a factor of 2, as discussed in Section 5.

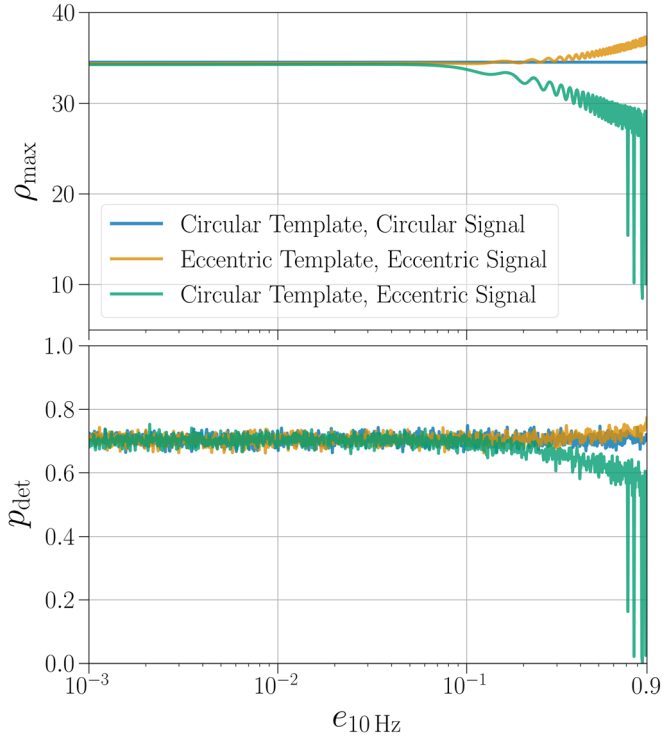

Figure 2. Time- and phase-maximized matched-filter S/N $\rho_{\rm max}$ (top panel) and detection probability $p_{\rm det}$ (bottom panel) over a range of $e_{10\,\rm Hz}$. For this demonstration, we use a fiducial zero-spin system with mass $m_1 = 36$ and $m_2 = 29\ M_\odot$, a luminosity distance $d_{\rm L} = 1$ Gpc, and a `midhighlatelow` PSD noise curve. The three colored curves represent the three signal–template combinations described in Section 3: a circular signal with a circular template (blue), an eccentric signal with an eccentric template (yellow), and an eccentric signal with a circular template (green). At high eccentricities ($e_{10\,\rm Hz} \gtrsim 0.1$), the time- and phase-maximized S/N slightly increases for the eccentric template/eccentric signal case, since the template can perfectly match the amplitude and phase modulations caused by eccentricity in the inspiral. It decreases for the circular template/eccentric signal case because of the mismatch between the template and the eccentric signal.

parameter estimation over a wide range of source parameters, we choose to adopt a fixed threshold eccentricity of $e_{\rm thresh} = 0.05$ for this analysis, where $e_{\rm thresh}$ is likewise defined at a reference GW frequency of 10 Hz. At this threshold, $\simeq$7% of the potentially detectable distribution of cluster binaries have $e_{10\,\rm Hz} > e_{\rm thresh}$. Our chosen value for $e_{\rm thresh}$ can be considered a lower limit, since weaker signals may require a higher threshold eccentricity to be distinguished from circular. However, small adjustments to this parameter do not impact our analysis significantly. For example, increasing $e_{\rm thresh}$ from 0.05 to 0.1 decreases the fraction of systems above this threshold by only $\lesssim$0.02. As described in the following section, increasing this threshold will decrease the fraction of detectable eccentric systems from dense star clusters, thereby increasing the branching fraction from clusters in the presence of an eccentric detection.

4. Implications of Eccentric Detections

Accounting for eccentricity in the selection effects afflicting the cluster population alters the detectable population. Under the assumption that matched-filter searches are the only means of detection (i.e., using circular templates for determining the detection probabilities, as shown with the green line in Figure 2), we find a steep decrease in recovered systems for $e_{10\,\rm Hz} \gtrsim 0.1$; see the inset of Figure 1. Using $e_{\rm thresh} = 0.05$ as the characteristic threshold for systems that will be measurably eccentric, we find that only 56% of potentially detectable systems with $e_{10\,\rm Hz} \geqslant e_{\rm thresh}$ will be recovered using matched-filter searches. Thus, measurably eccentric systems from clusters make up $\simeq$4% of the detectable distribution of BBH mergers from clusters. We refer to the fraction of measurably eccentric and detectable systems relative to the full detectable population as the detectable eccentric fraction $\xi_{\rm ecc}$, which allows us to translate the presence or absence of eccentric detections to information about the fraction of mergers taking place in dense clusters. For the following analyses, we use our calculated value of $\xi_{\rm ecc} = 3.9 \times 10^{-2}$.

Assuming dense star clusters account for a branching fraction $\beta_{\rm c}$ of the total number of observed BBH mergers and are the dominant contributor of eccentric sources, the probability of detecting $N_{\rm ecc}$ measurably eccentric systems given $N_{\rm obs}$ total BBH detections follows a homogeneous Poisson process,

$$p(N_{\rm ecc}|\lambda) = e^{-\lambda}\lambda^{N_{\rm ecc}}/N_{\rm ecc}!, \tag{1}$$

where

$$\lambda \equiv \xi_{\rm ecc}\beta_{\rm c}N_{\rm obs} \tag{2}$$

is the expected number of measurably eccentric detections after $N_{\rm obs}$ total observations. At a given $N_{\rm obs}$ and $N_{\rm ecc}$, we can determine the likelihood for the cluster branching fraction $\beta_{\rm c}$ by evaluating a grid of $\beta_{\rm c}$ in the cumulative distribution function (CDF) of Equation (1).

Constraints on $\beta_{\rm c}$ as a function of $N_{\rm obs}$ conditioned on various assumed measurably eccentric observations $N_{\rm ecc}$ are shown in Figure 3, with colored bands marking the symmetric 95% credible interval on $\beta_{\rm c}$. We plot unphysical values of $\beta_{\rm c} > 1$ as a posterior predictive check; though clusters cannot account for more than the entire observed population of BBHs, significant support for $\beta_{\rm c}$ in this region at a given $N_{\rm obs}$ and $N_{\rm ecc}$ indicates issues in the underlying cluster models due to the observation of too many eccentric systems.

We first consider the implications of not detecting measurably eccentric BBH mergers on the cluster branching fraction. At the number of BBH observations through the first half of the third observing run (O3a), the nondetection of a bona fide eccentric signal does not yet place tension on clusters dominating the detectable rate of BBHs; $\beta_{\rm c} = 1$ lies at the 83rd percentile of the likelihood. However, the nondetection of an eccentric signal will soon place interesting upper limits on the cluster branching fraction. At 100 (300) BBH observations, the lack of a bona fide eccentric signal will indicate $\beta_{\rm c} < 0.77$ (0.26) at 95% credibility. Once $\simeq$150 BBH observations have been made, the lack of a bona fide eccentric signal will indicate that clusters do not account for the majority of the detectable population ($\beta_{\rm c} < 0.5$).

No unambiguous eccentric detections have been found in the GW catalogs to date. However, multiple studies have found marginal to strong evidence that GW190521, one of the most massive BBH systems observed with GWs so far (Abbott et al. 2021b), is more consistent with being eccentric (Gayathri et al. 2020; Romero-Shaw et al. 2020, 2021) or from a hyperbolic encounter (Bustillo et al. 2021; Gamba et al. 2021) than a quasi-circular inspiral. Scattering experiments simulating the strong gravitational encounters typical of BHs in clusters indicate that GW190521-like binaries can enter the LIGO–Virgo band with

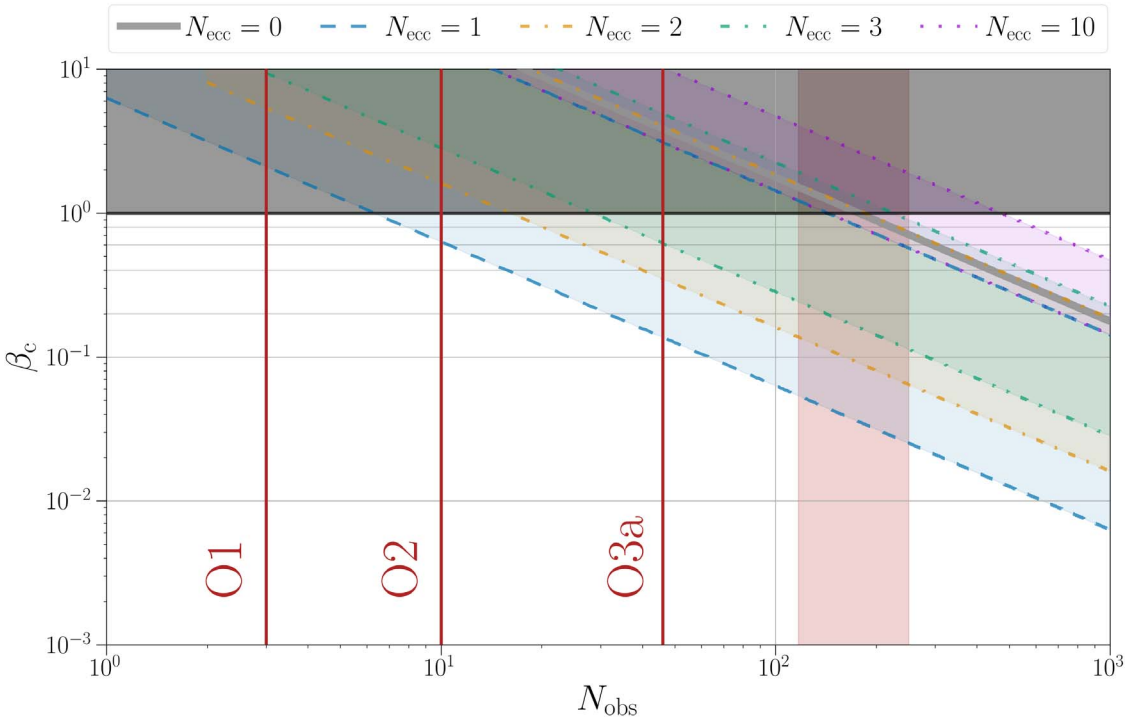

Figure 3. Constraints on the detectable branching fraction of dense star clusters, $\beta_{\rm c}$, as a function of the number of BBH observations, $N_{\rm obs}$, under the condition of $N_{\rm ecc}$ eccentric observations. For $N_{\rm ecc} = 0$, the solid gray diagonal line marks the upper 95th percentile of the $\beta_{\rm c}$ likelihood, and for $N_{\rm ecc} > 0$, colored bands encompass the 95% symmetric credible region of the $\beta_{\rm c}$ likelihood. We allow for branching fractions above the physical limit of $\beta_{\rm c} = 1$ in our likelihood (gray shaded region) to display combinations of $N_{\rm ecc}$ and $N_{\rm obs}$ that are unphysical, indicating issues with the underlying formation channel model or significant contamination from other eccentric channels. Red vertical lines mark the number of confident BBH observations reported so far in the first (O1), second (O2), and first half of the third (O3a) observing runs by the LVC. The red shaded region marks the predicted number of BBH observations after the fourth observing run (O4) from Abbott et al. (2018), assuming the second half of the third observing run observes the same number of BBH systems as O3a.

appreciable eccentricity (though not at extreme eccentricities of $e_{10\,\rm Hz} \gtrsim 0.7$; see Holgado et al. 2021). A detailed analysis investigating eccentricity in the BBH mergers from the second GW catalog (GWTC-2; Abbott et al. 2021b) also found evidence for eccentricity in the system GW190620A (Romero-Shaw et al. 2021).

Operating under the assumption that $N_{\rm ecc}$ out of the $N_{\rm obs} = 46$ BBH observations in GWTC-2 are measurably eccentric, we now focus on the constraints that can be placed on $\beta_{\rm c}$ given the presence of eccentric observations. Figure 4 shows the likelihood for $\beta_{\rm c}$ assuming different values of $N_{\rm ecc}$ at $N_{\rm obs} = 46$. Though the likelihood can have support at $\beta_{\rm c} > 1$, we also mark the >5% quantile of the posterior distribution with shaded regions, where we assume a flat-in-log prior with zero support above $\beta_{\rm c} > 1$, thus constraining $\beta_{\rm c}$ to its physically valid range. Given one (two) eccentric signal(s) in GWTC-2, one can place a lower limit on the detectable branching fraction of BBHs originating from clusters of 0.14 (0.27) at the 95% credible level.

An important diagnostic for determining the fidelity of the cluster models considered in this work is identifying the number of eccentric observations that would be infeasible at a given $N_{\rm obs}$. We quantify this by the likelihood volume that satisfies $\beta_{\rm c} \leqslant 1$, i.e., where there is nonzero prior probability. Given the number of BBH observations in GWTC-2, we find that there would be significant tension with eccentricity predictions from cluster models if $N_{\rm ecc} \geqslant 4$, as $\gtrsim$96% of the likelihood volume would be in the prior-excluded region. Observing this many eccentric mergers in the current catalog of BBH observations may also be an indication that a formation

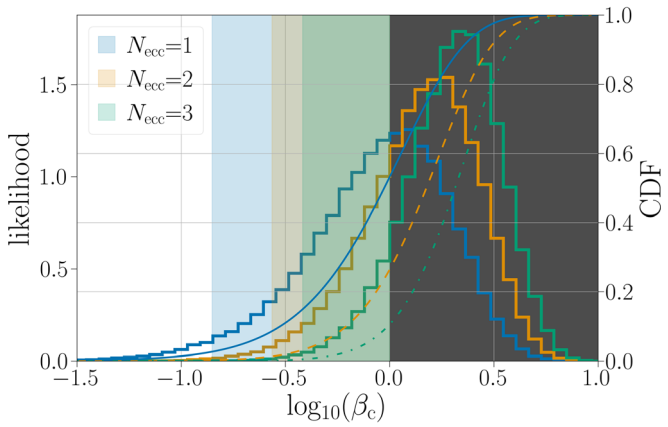

Figure 4. Constraints on the detectable branching fraction of the dense star cluster channel, $\beta_{\rm c}$, conditioned on $N_{\rm ecc}$ eccentric observations out of $N_{\rm obs} = 46$ total BBH observations. As with Figure 3, we show the likelihood (arbitrary units) without imposing the physical constraint of $\beta_{\rm c} \leqslant 1$ with solid lines and the corresponding CDF with dashed lines; the unphysical region $\beta_{\rm c} > 1$ is shaded in gray. Colored shaded regions mark the >5% quantile of the posterior distribution, in which we impose a flat-in-log prior on $\beta_{\rm c}$ with no support for $\beta_{\rm c} > 1$, and can be interpreted as a posteriori lower bounds on the cluster branching fraction given $N_{\rm ecc}$ eccentric observations. The relative location where the CDF crosses $\beta_{\rm c} = 1$ corresponds to the evidence of models in which $N_{\rm ecc}$ eccentric BBH systems are observed given 46 total BBH observations.

channel other than dense stellar clusters is significantly contributing to the eccentric BBH population.

As $N_{\rm ecc}$ grows, tighter constraints on $\beta_{\rm c}$ are achieved, since the width of the $\log_{10}(\beta_{\rm c})$ likelihood is independent of $N_{\rm obs}$. At $N_{\rm ecc} = 1$ (3), the symmetric 95% credible region for $\beta_{\rm c}$ is

constrained to 1.36 (0.90) dex. Precision of ≈0.5 dex for the 95% credible range on β_c will be achieved at $N_{ecc} \gtrsim 10$.

5. Discussion and Conclusions

In this work, we show how the detection or nondetection of measurably eccentric GW sources can act to significantly constrain the contribution of certain dynamical channels to the detectable BBH population. Our main results are as follows.

1. Dense star cluster models robustly predict that ≈7% of potentially detectable sources will be measurably eccentric, though matched-filter searches will only recover ≈56% of this cluster subpopulation.
2. Though the nondetection of a measurably eccentric source in GWTC-2 would not rule out the hypothesis that clusters are the dominant contributor of detectable sources, once 150 BBH observations have been made, the lack of a bona fide eccentric observation would indicate that clusters do not make up more than 50% of the detectable population of BBHs. Even with pessimistic predictions, this number of BBH mergers will be reached in O4.
3. Assuming that it originated in a dense star cluster, a single measurably eccentric source in GWTC-2 would indicate that such clusters account for >14% of the detectable BBH population.
4. Once 10 eccentric observations from clusters have been made, the detectable branching fraction from clusters will be constrained at the 0.5 dex level.

Eccentricity may be the most robust indicator of a dynamical BBH formation pathway, as the presence of eccentric mergers in clusters is relatively insensitive to uncertain physical processes that impact other dynamical indicators, such as binary evolution physics, the efficiency of angular momentum transport in massive stars, and the location of the pair instability mass gap. Instead, eccentric mergers in dynamical environments are the result of well-understood physics, and if BHs are indeed present in clusters, eccentric mergers are an inevitable by-product.

Current state-of-the-art models of dense star clusters predict local BBH merger rates of ∼2–20 $\mathrm{Gpc^{-3}\,yr^{-1}}$ (Kremer et al. 2020; Rodriguez et al. 2021). Based on this work, this would translate to a merger rate of measurably eccentric sources of ∼0.08–0.8 $\mathrm{Gpc^{-3}\,yr^{-1}}$. However, this translation depends on the fraction of GW captures relative to all BBH mergers in clusters, which in the local universe is sensitive to the initial density distribution of clusters. Though our cluster models have initial densities tuned to reproducing the density profiles of clusters observed in the Milky Way today, the Milky Way's cluster population may not be representative of the local universe as a whole (e.g., Jordán et al. 2015), and for high initial cluster densities ($\gtrsim 10^5\ M_\odot\,\mathrm{pc^{-3}}$), the fraction of local GW captures may reduce by a factor of ∼2–3 (Antonini & Gieles 2020a). Other model variations, such as metallicity distributions, cluster formation times, binary physics, and remnant formation prescriptions, have a much more minor effect on the fraction of in-cluster mergers and local GW captures (see Table 1 of Antonini & Gieles 2020a). Reducing the local GW capture fraction (i.e., reducing ξ_{ecc}) would act to increase our recovered values of β_c, thereby making our lower limits on cluster branching fractions conservative. However, it is important to note that possible systematics can only vary the value of ξ_{ecc} by a factor of a few, and no reasonable model variations can cause this eccentric population to disappear entirely, which makes eccentric signals in clusters a robust prediction compared to most other predictions from population modeling.

The predicted merger rate from dense star clusters is comparable to the empirically measured rate by the LIGO Scientific Collaboration and Virgo Collaboration (LVC) following GWTC-2 of 15–39 $\mathrm{Gpc^{-3}\,yr^{-1}}$ (90% credibility; Abbott et al. 2021a). However, it is likely that GCs only account for a portion of this rate, and the diversity of BBH observations to date hint at multiple formation channels contributing significantly to the observed population of BBHs (Abbott et al. 2021a; Zevin et al. 2021). Since eccentric sources will be extremely useful for constraining the merger rate from clusters, they will also assist in limiting the rate contribution of other formation channels.

This analysis estimates eccentric detectability assuming only matched-filter searches with circular, aligned-spin templates. Though these searches are the main workhorse for the detection of compact binary coalescences, a number of other search techniques are used to identify GW signals. Of particular pertinence to this study are burst searches, which are unmodeled searches that identify coincident and coherent signals in the GW data stream. For nearby and loud mergers, burst searches would excel over quasi-circular template-based searches at detecting highly eccentric systems (Klimenko et al. 2016). A possible example of this in action is GW190521, which was found by a burst search to have a much lower false-alarm rate (<1 per 28 yr) than reported for the same candidate by matched-filter compact binary pipelines (⩾1 per 8 yr; Abbott et al. 2020). In addition, higher matched-filter S/Ns may be achieved by marginalizing over the intrinsic parameters of the template rather than considering a single circular template with analogous source properties. Thus, the detectable eccentric fraction ξ_{ecc} we report can be considered a lower limit. However, if one were to assume the limiting case, where eccentric mergers are equally as likely to be detected as their circular counterparts, the maximum detectable eccentric fraction would be less than twice our reported value. Therefore, even in this best-case detectability scenario, our constraints on branching fractions as a function of the number of BBH observations are reduced by less than a factor of 2.

We also assume that strong gravitational encounters in clusters are the only means of generating measurably eccentric mergers in the LIGO–Virgo sensitive frequency range. Other formation channels have been proposed for generating systems with measurable eccentricities, though the predicted local merger rates and/or eccentricity distributions for these channels are typically subject to more uncertainties, as they are not solely a simple by-product of two-body relaxation and small-N dynamics.

1. In the secular evolution of isolated hierarchical systems, predicted merger rates for measurably eccentric systems in the LIGO–Virgo band are at most ∼0.1 $\mathrm{Gpc^{-3}\,yr^{-1}}$ (Antonini et al. 2017), but they are sensitive to initial orbital properties and rely on BHs having no natal kicks, dropping 1–2 orders of magnitude if even weak natal kicks are assumed (Silsbee & Tremaine 2017; Rodriguez & Antonini 2018).
2. Perturbations of field triples by flyby encounters may also contribute significantly with a measurable eccentric

merger rate of up to $\sim$1–10 $\mathrm{Gpc}^{-3}\,\mathrm{yr}^{-1}$ (Michaely & Perets 2020), though this channel is also highly sensitive to BH natal kicks and initial binary properties, and the impact of these parameterizations on the predicted merger rate has yet to be explored.

3. For BBH systems in binaries or triples orbiting supermassive BHs, the predicted merger rates for measurably eccentric BBHs range from $\sim$0.03 to 0.16 $\mathrm{Gpc}^{-3}\,\mathrm{yr}^{-1}$ (Fragione et al. 2019) and are dependent on the supermassive BH and stellar mass BH mass functions, as well as the initial orbital semimajor axis and eccentricity distribution of BBHs; these rates can be further enhanced by asphericity in the nuclear cluster itself (Petrovich & Antonini 2017).
4. Single–single captures in galactic nuclei are a promising avenue for detectable eccentric mergers, with $\gtrsim$90% of systems exhibiting potentially measurable signs of eccentricity (Gondán & Kocsis 2021). Furthermore, this channel is relatively insensitive to initial condition and binary evolution uncertainties such as the BH mass function, though the overall merger rate of this channel ranges from $\sim$0.002 to 0.04 $\mathrm{Gpc}^{-3}\,\mathrm{yr}^{-1}$ and is exponentially sensitive to the radial number density profile exponent for galactic nuclei (Rasskazov & Kocsis 2019).
5. Lastly, though predicted rates for BBH mergers in active galactic nucleus (AGN) disks span many orders of magnitude (Gröbner et al. 2020; McKernan et al. 2020), a substantial number ($\gtrsim$10%) of mergers in AGN disks may show measurable signs of eccentricity, with this percentage possibly increasing to $\sim$70% if BHs are contained to the disk or can migrate to within 10^{-3} pc of the supermassive BH (Tagawa et al. 2021; Samsing et al. 2020b).[12]

Despite the higher degree of uncertainty inherent to many of these eccentric BBH channels, if they contribute significantly to the measurably eccentric merger rate, the inclusion of these channels would impact the branching fraction constraints for the dense star clusters reported in this work. Robust rate estimates and eccentricity distributions from these channels could be incorporated into the methodology presented here, allowing for mixture models to be created with multiple eccentric detection efficiencies and joint constraints on the contribution of formation channels that generate eccentric BBH mergers.

The utility of eccentric detections for constraining formation channels will improve as more BBH mergers are observed, regardless of whether or not eccentric mergers are observed in this population. The eccentric detection efficiency will also be relatively stable as the sensitivity of the detector network improves, as the fraction of measurably eccentric mergers relative to the full cluster population does not evolve significantly with redshift (Rodriguez et al. 2018a). Given current BBH rate measurements and the anticipated sensitivity of the GW detector network in O4, the lack of a measurably eccentric detection after O4 will indicate that clusters do not account for the majority of BBH mergers. On the other hand, with future eccentric detections, we will significantly constrain the lower limit of mergers that result from clusters and other dynamical channels. Once $\sim$10 eccentric BBH mergers are observed, constraints on the dynamical branching fraction will reach the 0.5 dex level, potentially making eccentricity the most robust and efficient means for constraining the formation pathways of BBH mergers.

We thank Rossella Gamba for useful comments on this manuscript, Carl Rodriguez for assistance in computing the relative weights for the CMC cluster models, Fabio Antonini and Mark Gieles for interesting discussions regarding uncertainties in initial cluster densities, Daniel Holz for enlightening discussions, and Alessandro Nagar, Sebastiano Bernuzzi, and Piero Rettegno for help with and development of the TEOBResumS waveform model. We also thank the anonymous referee, whose comments and suggestions improved this manuscript. Support for this work and for M.Z. was provided by NASA through NASA Hubble Fellowship grant HST-HF2-51474.001-A awarded by the Space Telescope Science Institute, which is operated by the Association of Universities for Research in Astronomy, Inc., for NASA, under contract NAS5-26555. K.K. is supported by an NSF Astronomy and Astrophysics Postdoctoral Fellowship under award AST-2001751. E.T. and P.D.L. are supported through Australian Research Council (ARC) Centre of Excellence CE170100004. P.D.L. is supported through ARC Future Fellowship FT160100112 and ARC Discovery project DP180103155. This work used computing resources at CIERA funded by NSF grant No. PHY-1726951 and resources and staff provided by the Quest high-performance computing facility at Northwestern University, which is jointly supported by the Office of the Provost, the Office for Research, and Northwestern University Information Technology.

Software: Astropy (Robitaille et al. 2013; Price-Whelan et al. 2018); iPython (Pérez & Granger 2007); Matplotlib (Hunter 2007); NumPy (Oliphant 2006; Van Der Walt et al. 2011); Pandas (McKinney 2010); PyCBC (Nitz et al. 2019); SciPy (Virtanen et al. 2020); TEOBResumS (Nagar et al. 2018).

Appendix A
Cluster Models and Eccentricity of BBH Sources

We obtain our sample of BBHs from the 148 *N*-body cluster simulations in Kremer et al. (2020). In each cluster model, the component masses, component spin magnitudes, and merger redshifts of BBH mergers are recorded. The BHs are assumed to have negligible birth spin, as predicted if angular momentum transport in their massive-star progenitors is highly efficient (Spruit 1999, 2002; Fuller et al. 2019), though spin can be imparted in cluster BHs through prior BBH merger events that are retained in the cluster. Spin tilts are assumed to be isotropically distributed on the sphere. The BBHs in our models have (source-frame) total masses between 14 and 135 $M_\odot$, mass ratios between 0.3 and 1.0, and effective spins between -0.42 and 0.42, where the quoted ranges represent 99% of all systems.

In order to obtain an appropriate astrophysically weighted sample of BBHs from the Kremer et al. (2020) models, we follow the approach described in Rodriguez & Loeb (2018) and Martinez et al. (2021). To briefly summarize, the 148 cluster models from Kremer et al. (2020) are placed into equally spaced bins in cluster mass and logarithmically spaced bins in metallicity. Each cluster model is then assigned a relative astrophysical weight, γ_c, corresponding to the number of

[12] We note that, based on our analysis, the high efficiency of eccentric mergers predicted from the galactic nuclei and AGN disk channels combined with only $\sim$zero to two eccentric mergers in GWTC-2 (e.g., Romero-Shaw et al. 2021) may indicate that these channels are a subdominant contributor to the total BBH merger rate if the predicted eccentricity distributions are similar to those of dense star clusters.

clusters that are thought to form in that 2D bin across cosmic time. Initial cluster masses are assumed to follow an M^{-2} distribution (e.g., Lada & Lada 2003), and metallicities are obtained from El-Badry et al. (2019). A formation time for each cluster is also drawn from the metallicity-dependent formation time distributions from El-Badry et al. (2019). The cluster formation time, $t_{\rm form}$, drawn for a given cluster model is then added to the merger times, $t_{\rm merge}$, for all BBH mergers identified in that model. Systems with $t_{\rm form}+t_{\rm merge}$ larger than a Hubble time are excluded from the analysis.

The orbital integration of merging BBHs is halted once the component BHs reach a separation of $10\,M$, where M is the total mass of the binary in geometric units, and the semimajor axis and eccentricity of the orbit are recorded at various discrete separations prior to this point (see Rodriguez et al. 2018a for further discussion on halting criteria). To acquire the orbital properties at a particular GW frequency $f_{\rm GW}$ for a binary of total mass $M_{\rm tot}$, we use the orbital properties recorded at a separation of $100\,M$ and numerically solve for the orbital properties at an eccentric peak frequency as in Wen (2003),

$$a(e)=\frac{1}{1-e^2}\left[\frac{GM_{\rm tot}}{\pi}\frac{(1+e)^{1.1954}}{f_{\rm GW}}\right]^{2/3}, \tag{A1}$$

which is coupled to the differential equation governing the coevolution of semimajor axis and eccentricity from Peters (1964):

$$\left\langle\frac{da}{de}\right\rangle=\frac{12}{19}\frac{a}{e}\frac{[1+(73/24)e^2+(37/96)e^4}{(1-e^2)[1+(121/304)e^2]}. \tag{A2}$$

In certain cases, the binary forms through a hyperbolic capture at frequencies above $f_{\rm GW}$, and we assign its eccentricity at $f_{\rm GW}$ to an extremal value of $e_{\rm max}=0.9$.

As we are interested in the properties of detectable BBH mergers rather than the underlying population, we must also account for the larger amount of comoving volume accessible at higher redshifts and the relative sensitivity of GW detectors to BBHs with different properties. Each system i, parameterized by component masses m_1 and m_2, component spin vectors χ_1 and χ_2, merger redshift z, eccentricity at a reference frequency of 10 Hz $e_{10\,\rm Hz}$, and cluster weight $\gamma_{\rm c}$, is given a normalized detectability weight of

$$w_i=\left[\gamma_{\rm c}\frac{dVc}{dz}\frac{dt_s}{dt_0}p_{\rm det}(m_1,m_2,\chi_1,\chi_2,e_{10\,\rm Hz},z)\right]_i, \tag{A3}$$

where $\frac{dVc}{dz}$ is the comoving volume element at redshift z, $\frac{dt_s}{dt_0}=(1+z)^{-1}$ is the time dilation between clocks at the merger redshift and on Earth, and $p_{\rm det}$ is the detection probability of a system with a given set of intrinsic parameters, defined in the following section.

Appendix B
Detectability of Eccentric Sources

We estimate detection probabilities using a fixed S/N threshold required for detection of $\rho_{\rm thresh}=8.0$. Given the source parameters of each system, we calculate a matched-filter S/N assuming the optimal orientation of face-on and directly overhead,

$$\rho^2_{\rm max}=\frac{1}{\langle h|h\rangle}|\langle s|h\rangle|^2, \tag{B1}$$

where we maximize over the phase and time of coalescence, and $\langle s|h\rangle$ is the noise-weighted inner product,

$$\langle s|h\rangle=4\int_0^\infty\frac{\tilde{s}(f)\tilde{h}^\star(f)}{S_n(f)}df, \tag{B2}$$

with $\tilde{s}(f)$ and $\tilde{h}(f)$ being the Fourier transform of the time-domain signal and template, respectively, and $S_n(f)$ the one-sided average power spectral density (PSD) of the detector noise. The noise-weighted inner product of the template with itself $\langle h|h\rangle$ is the optimal matched-filter S/N and defined similarly. We assume a stationary, single-detector LIGO PSD with `midhighlatelow` sensitivity from Abbott et al. (2018), which has been shown to be a decent approximation to the more sophisticated approach of injection/recovery campaigns in search pipelines (e.g., Abbott et al. 2018; Nitz et al. 2020).

For the three matched-filter cases described in Section 3, we window the waveforms with a Tukey filter, and in cases where the signal and template are not identical, we zero-pad the shorter waveform, time-align the maximum strain of the template and signal, and apply a frequency-domain time and phase shift determined by maximizing the overlap integral. If $\rho_{\rm max}<\rho_{\rm thresh}$, the detection probabilities are assigned to be zero. Otherwise, we determine the detection probabilities by Monte Carlo sampling uniformly over the extrinsic parameters ψ and multiplying the maximized S/N with the detector projection factor $\Theta(\psi)\in[0,1]$ (Finn & Chernoff 1993). The detection probability is thus determined as

$$p_{\rm det}=\sum_{j=1}^{N}\mathcal{H}[\Theta(\psi_j)\rho_{\rm max}-\rho_{\rm thresh}], \tag{B3}$$

where $\mathcal{H}$ is the Heaviside step function, and we draw $N=10^3$ sets of extrinsic parameters.

ORCID iDs

Michael Zevin https://orcid.org/0000-0002-0147-0835
Isobel M. Romero-Shaw https://orcid.org/0000-0002-4181-8090
Kyle Kremer https://orcid.org/0000-0002-4086-3180
Eric Thrane https://orcid.org/0000-0002-4418-3895
Paul D. Lasky https://orcid.org/0000-0003-3763-1386

References

Aasi, J., Abbott, B. P., Abbott, R., et al. 2015, CQGra, 32, 074001
Abbott, B. P., Abbott, R., Abbott, T. D., et al. 2016, PhRvL, 116, 061102
Abbott, B. P., Abbott, R., Abbott, T. D., et al. 2018, LRR, 21, 3
Abbott, B. P., Abbott, R., Abbott, T. D., et al. 2019a, ApJ, 883, 149
Abbott, B. P., Abbott, R., Abbott, T. D., et al. 2019b, PhRvX, 9, 31040
Abbott, R., Abbott, T. D., Abraham, S., et al. 2020, PhRvL, 125, 101102
Abbott, R., Abbott, T. D., Abraham, S., et al. 2021a, ApJL, 913, L7
Abbott, R., Abbott, T. D., Abraham, S., et al. 2021b, PhRvX, 11, 021053
Acernese, F., Agathos, M., Agatsuma, K., et al. 2015, CQGra, 32, 024001
Adams, T., Buskulic, D., Germain, V., et al. 2016, CQGra, 33, 175012
Ade, P. A., Aghanim, N., Arnaud, M., et al. 2016, A&A, 594, A13
Albanesi, S., Nagar, A., & Bernuzzi, S. 2021, PhRvD, 104, 024067
Allen, B., Anderson, W. G., Brady, P. R., Brown, D. A., & Creighton, J. D. 2012, PhRvD, 85, 122006
Antognini, J. M., Shappee, B. J., Thompson, T. A., & Amaro-seoane, P. 2014, MNRAS, 439, 1079

Antonini, F., & Gieles, M. 2020a, PhRvD, 102, 123016
Antonini, F., & Gieles, M. 2020b, MNRAS, 492, 2936
Antonini, F., & Perets, H. B. 2012, ApJ, 757, 27
Antonini, F., Toonen, S., & Hamers, A. S. 2017, ApJ, 841, 77
ArcaSedda, M., Askar, A., Giersz, M., et al. 2018, MNRAS, 479, 4652
Aubin, F., Brighenti, F., Chierici, R., et al. 2021, CQGra, 38, 095004
Banerjee, S. 2017, MNRAS, 467, 524
Bartos, I., Kocsis, B., Haiman, Z., & Márka, S. 2017, ApJ, 835, 165
Bavera, S. S., Fragos, T., Zevin, M., et al. 2021, A&A, 647, A153
Belczynski, K., Holz, D. E., Bulik, T., & O'shaughnessy, R. 2016, Natur, 534, 512
Bethe, H. A., & Brown, G. E. 1998, ApJ, 506, 780
Bird, S., Cholis, I., Muñoz, J. B., et al. 2016, PhRvL, 116, 201301
Bouffanais, Y., Mapelli, M., Santoliquido, F., et al. 2021, MNRAS, 507, 5224
Breen, P. G., & Heggie, D. C. 2013, MNRAS, 436, 584
Buonanno, A., & Damour, T. 1999, PhRvD, 59, 084006
Buonanno, A., & Damour, T. 2000, PhRvD, 62, 064015
Bustillo, J. C., Sanchis-Gual, N., Torres-Forné, A., et al. 2021, PhRvL, 126, 201101
Chatterjee, S., Rodriguez, C. L., Kalogera, V., & Rasio, F. A. 2017, ApJL, 836, L26
Chiaramello, D., & Nagar, A. 2020, PhRvD, 101, 101501
Chu, Q., Kovalam, M., Wen, L., et al. 2020, arXiv:2011.06787
Clesse, S., & Garcia-Bellido, J. 2020, arXiv:2007.06481
Dal Canton, T., Nitz, A. H., Lundgren, A. P., et al. 2014, PhRvD, 90, 082004
Damour, T. 2001, PhRvD, 64, 124013
Damour, T., Jaranowski, P., & Schäfer, G. 2000, PhRvD, 62, 084011
Damour, T., Jaranowski, P., & Schäfer, G. 2015, PhRvD, 91, 084024
Damour, T., & Nagar, A. 2014, PhRvD, 90, 044018
Davies, G. S., Dent, T., Tápai, M., et al. 2020, PhRvD, 102, 22004
Di Carlo, U. N., Giacobbo, N., Mapelli, M., et al. 2019, MNRAS, 487, 2947
Dominik, M., Belczynski, K., Fryer, C., et al. 2012, ApJ, 759, 52
Downing, J. M. B., Benacquista, M. J., Giersz, M., & Spurzem, R. 2010, MNRAS, 407, 1946
El-Badry, K., Quataert, E., Weisz, D. R., Choksi, N., & Boylan-Kolchin, M. 2019, MNRAS, 482, 4528
Finn, L. S., & Chernoff, D. F. 1993, PhRvD, 47, 2198
Fragione, G., & Bromberg, O. 2019, MNRAS, 488, 4370
Fragione, G., Grishin, E., Leigh, N. W. C., Perets, H. B., & Perna, R. 2019, MNRAS, 488, 2825
Fragione, G., & Kocsis, B. 2018, PhRvL, 121, 161103
Fragione, G., & Kocsis, B. 2019, MNRAS, 486, 4781
Franciolini, G., Baibhav, V., De Luca, V., et al. 2021, arXiv:2105.03349
Fregeau, J. M., Cheung, P., Zwart, S. F. P., & Rasio, F. A. 2004, MNRAS, 352, 1
Fregeau, J. M., & Rasio, F. A. 2007, ApJ, 658, 1047
Fuller, J., Piro, A. L., & Jermyn, A. S. 2019, MNRAS, 485, 3661
Gamba, R., Breschi, M., Carullo, G., et al. 2021, arXiv:2106.05575
Gayathri, V., Healy, J., Lange, J., et al. 2020, arXiv:2009.05461
Giesers, B., Dreizler, S., Husser, T. O., et al. 2018, MNRAS, 475, L15
Giesers, B., Kamann, S., Dreizler, S., et al. 2019, A&A, 632, A3
Gondán, L., & Kocsis, B. 2021, MNRAS, 506, 1665
Gondán, L., Kocsis, B., Raffai, P., & Frei, Z. 2018, ApJ, 860, 5
Gröbner, M., Ishibashi, W., Tiwari, S., Haney, M., & Jetzer, P. 2020, A&A, 638, A119
Holgado, A. M., Ortega, A., & Rodriguez, C. L. 2021, ApJL, 909, L24
Hooper, S., Chung, S. K., Luan, J., et al. 2012, PhRvD, 86, 024012
Hunter, J. D. 2007, CSE, 9, 99
Jordán, A., Peng, E. W., Blakeslee, J. P., et al. 2015, ApJS, 221, 13
Klimenko, S., Vedovato, G., Drago, M., et al. 2016, PhRvD, 93, 042004
Kocsis, B., & Levin, J. 2012, PhRvD, 85, 123005
Kremer, K., Chatterjee, S., Ye, C. S., Rodriguez, C. L., & Rasio, F. A. 2019, ApJ, 871, 38
Kremer, K., Ye, C. S., Chatterjee, S., Rodriguez, C. L., & Rasio, F. A. 2018, ApJL, 855, L15
Kremer, K., Ye, C. S., Rui, N. Z., et al. 2020, ApJS, 247, 48
Lada, C. J., & Lada, E. A. 2003, ARA&A, 41, 57
Liu, B., & Lai, D. 2019, MNRAS, 483, 4060
Liu, B., Lai, D., & Wang, Y.-H. 2019, ApJ, 881, 41
Loutrel, N. 2020, arXiv:2009.11332
Lower, M. E., Thrane, E., Lasky, P. D., & Smith, R. 2018, PhRvD, 98, 083028
Mackey, A. D., Wilkinson, M. I., Davies, M. B., & Gilmore, G. F. 2007, MNRAS, 379, 40
Martinez, M. A. S., Rodriguez, C. L., & Fragione, G. 2021, arXiv:2105.01671
McKernan, B., Ford, K. E., Kocsis, B., Lyra, W., & Winter, L. M. 2014, MNRAS, 441, 900
McKernan, B., Ford, K. E. S., & O'Shaughnessy, R. 2020, MNRAS, 498, 4088
McKinney, W. 2010, in Proc. 9th Python in Science Conf., Data Structures for Statistical Computing in {P}ython, ed. S. van der Walt & J. Millman (SciPy), 51
Messick, C., Blackburn, K., Brady, P., et al. 2017, PhRvD, 95, 042001
Michaely, E., & Perets, H. B. 2019, ApJL, 887, L36
Michaely, E., & Perets, H. B. 2020, MNRAS, 498, 4924
Nagar, A., Bernuzzi, S., Del Pozzo, W., et al. 2018, PhRvD, 98, 104052
Nagar, A., Bonino, A., & Rettegno, P. 2021, PhRvD, 103, 104021
Nitz, A., Harry, I., Brown, D., et al. 2019, gwastro/pycbc: PyCBC Release v1.14.4, Zenodo, doi:10.5281/zenodo.3546372
Nitz, A. H., Dent, T., Dal Canton, T., Fairhurst, S., & Brown, D. A. 2017, ApJ, 849, 118
Nitz, A. H., Schäfer, M., & Canton, T. D. 2020, ApJL, 902, L29
O'Leary, R. M., Kocsis, B., & Loeb, A. 2009, MNRAS, 395, 2127
O'Leary, R. M., Rasio, F. A., Fregeau, J. M., Ivanova, N., & O'Shaughnessy, R. 2006, ApJ, 637, 937
Oliphant, T. E. 2006, A guide to NumPy (USA: Trelgol Publishing)
Pérez, F., & Granger, B. E. 2007, CSE, 9, 21
Peters, P. C. 1964, PhRv, 136, 1224
Petrovich, C., & Antonini, F. 2017, ApJ, 846, 146
PortegiesZwart, S. F., & McMillan, S. L. W. 2000, ApJL, 528, 17
Price-Whelan, A. M., Sipocz, B. M., Günther, H. M., et al. 2018, AJ, 156, 123
Ramos-Buades, A., Tiwari, S., Haney, M., & Husa, S. 2020, PhRvD, 102, 43005
Rasskazov, A., & Kocsis, B. 2019, ApJ, 881, 20
Robitaille, T. P., Tollerud, E. J., Greenfield, P., et al. 2013, A&A, 558, A33
Rodriguez, C. L., Amaro-seoane, P., Chatterjee, S., et al. 2018a, PhRvD, 98, 123005
Rodriguez, C. L., Amaro-Seoane, P., Chatterjee, S., & Rasio, F. A. 2018b, PhRvL, 120, 151101
Rodriguez, C. L., & Antonini, F. 2018, ApJ, 863, 7
Rodriguez, C. L., Chatterjee, S., & Rasio, F. A. 2016, PhRvD, 93, 084029
Rodriguez, C. L., Kremer, K., Chatterjee, S., et al. 2021, RNAAS, 5, 19
Rodriguez, C. L., & Loeb, A. 2018, ApJL, 866, L5
Romero-Shaw, I., Lasky, P. D., Thrane, E., & Calderón Bustillo, J. 2020, ApJL, 903, L5
Romero-Shaw, I. M., Lasky, P. D., & Thrane, E. 2019, MNRAS, 490, 5210
Romero-Shaw, I. M., Lasky, P. D., & Thrane, E. 2021, arXiv:2108.01284
Samsing, J. 2018, PhRvD, 97, 103014
Samsing, J., Askar, A., & Giersz, M. 2018, ApJ, 855, 124
Samsing, J., Bartos, I., D'Orazio, D. J., et al. 2020b, arXiv:2010.09765
Samsing, J., D'Orazio, D. J., Kremer, K., Rodriguez, C. L., & Askar, A. 2020a, PhRvD, 101, 123010
Samsing, J., MacLeod, M., & Ramirez-Ruiz, E. 2014, ApJ, 784, 71
Samsing, J., & Ramirez-Ruiz, E. 2017, ApJL, 840, L14
Sasaki, M., Suyama, T., Tanaka, T., & Yokoyama, S. 2018, CQGra, 35, 063001
Silsbee, K., & Tremaine, S. 2017, ApJ, 836, 39
Spruit, H. C. 1999, A&A, 349, 189
Spruit, H. C. 2002, A&A, 381, 923
Stone, N. C., Metzger, B. D., & Haiman, Z. 2017, MNRAS, 464, 946
Strader, J., Chomiuk, L., MacCarone, T. J., Miller-Jones, J. C., & Seth, A. C. 2012, Natur, 490, 71
Tagawa, H., Kocsis, B., Haiman, Z., et al. 2021, ApJL, 907, L20
Takatsy, J., Bécsy, B., & Raffai, P. 2019, MNRAS, 486, 570
Tiwari, V., Klimenko, S., Christensen, N., et al. 2016, PhRvD, 93, 043007
Usman, S. A., Nitz, A. H., Harry, I. W., et al. 2016, CQGra, 33, 215004
van der Walt, S., Colbert, S. C., Varoquaux, G., et al. 2011, CSE, 13, 22
Virtanen, P., Gommers, R., Oliphant, T. E., et al. 2020, Nat. Methods, 17, 261
Wang, L., Spurzem, R., Aarseth, S., et al. 2016, MNRAS, 458, 1450
Weatherford, N. C., Chatterjee, S., Kremer, K., & Rasio, F. A. 2020, ApJ, 898, 162
Wen, L. 2003, ApJ, 598, 419
Wong, K. W. K., Franciolini, G., Luca, V. D., et al. 2021, PhRvD, 103, 23026
Zevin, M., Bavera, S. S., Berry, C. P., et al. 2021, ApJ, 910, 152
Zevin, M., Samsing, J., Rodriguez, C., Haster, C.-J., & Ramirez-Ruiz, E. 2019, ApJ, 871, 91